

# The single atom Fe loaded catalytic membrane for effective peroxyomonosulfate activation and pollution degradation



Ruonan Guo<sup>a,c</sup>, Changsheng Guo<sup>a</sup>, Zenghui Bi<sup>b</sup>, Heng Zhang<sup>a</sup>, Ningqing Lv<sup>a</sup>, Beidou Xi<sup>a,c</sup>, Guangzhi Hu<sup>b</sup>, Jian Xu<sup>a,\*</sup>

<sup>a</sup> State Key Laboratory of Environmental Criteria and Risk Assessment, Chinese Research Academy of Environmental Sciences, Beijing 100012, China

<sup>b</sup> Institute for Ecological Research and Pollution Control of Plateau Lakes, School of Ecology and Environmental Science, Yunnan University, Kunming 650504, China

<sup>c</sup> School of Environment, Tsinghua University, Beijing 100084, China

## ARTICLE INFO

### Keywords:

Fenton-like  
Single atom catalysts  
Membrane  
Nitenpyram degradation  
Density functional theory

## ABSTRACT

A novel iron-based single-atom catalyst (Fe SAC) integrated into a catalytic membrane was developed for peroxyomonosulfate (PMS) activation and organic pollutant degradation. The Fe SAC membrane was synthesized using a co-precipitation method and acid leaching treatment, and its catalytic activity was evaluated in a continuous flow-through system using nitenpyram (NPR) as a model pollutant. The Fe SAC membrane/PMS system achieved over 90% NPR removal efficiency with low iron leaching (2.85–8.05 µg/L) during 10 hours of continuous operation, and maintained over 80% NPR removal in tap water, Yellow River water, and Yangtze River water. Experimental and theoretical analyses revealed that the strong chemisorption and electron transfer between PMS and FeN4 led to the dominant production of singlet oxygen for NPR degradation. This study demonstrates the potential of SAC-based catalytic membranes for efficient and stable attenuation of refractory organic pollutants in water treatment applications.

## 1. Introduction

Persulfate-based advanced oxidation processes (persulfate-AOPs) are emerging as powerful techniques for water treatment, particularly effective against refractory organic pollutants [1–3]. Nanomaterials have provided immense impetus as heterogeneous catalysts to activate peroxyomonosulfate (PMS) [4,5]. It is widely acknowledged that the key to achieving effective persulfate activation for removing refractory pollutants is the development of catalysts that are highly active, stable, and cost-efficient [1,6]. Traditional metal nanoparticle catalysts, while potent, are plagued by challenges such as loss of catalyst into product water, mass transfer resistance, and vulnerability to structural damage under intense shear forces [7,8]. These limitations hinder the widespread application of persulfate-AOPs in practical water treatment processes. To overcome these obstacles, single-atom catalysts (SACs) have been developed. SACs involve metal catalysts anchored to a substrate via strong ligand bonds and dispersed atomically, thereby preventing metal–metal interactions and fully exposing each atom to the reaction environment [9]. This unique configuration maximizes the utilization of metal active sites and enhances surface energy, positioning

SACs as an optimal intermediary between homogeneous and heterogeneous catalysts [10,11]. SACs present another advantage of enhanced stability under harsh reaction conditions and are less prone to damage from intense shear forces. Despite these advancements, challenges remain in heterogeneous catalytic systems, including the loss of catalyst particles to product water, limitations in mass transfer, and susceptibility to oxidative degradation by reactive oxygen species (ROS) under strenuous conditions [12]. This underscores the need for ongoing research and development to refine the design and application of SACs in water treatment processes.

To enhance the performance of persulfate-AOPs while circumventing issues related to catalyst separation, methodologies such as membrane-based reaction systems and electrocatalytic auxiliary systems have been proposed for the immobilization of powder catalysts [7]. Nevertheless, the specially designed reactors are required in electrocatalytic auxiliary systems. The membrane filtration technology not only provides abundant sites for catalyst immobilization, but also promotes effective contact between reactants and catalysts through forced convection in the membrane pores [13,14]. It is crucial to recognize that the ROS generated during PMS activation are short-lived, with

\* Corresponding author.

E-mail address: [xujian@craes.org.cn](mailto:xujian@craes.org.cn) (J. Xu).

half-lives of less than 10  $\mu$ s for hydroxyl radical ( $\bullet\text{OH}$ ), 30–40  $\mu$ s for sulfate radical ( $\text{SO}_4^{\bullet-}$ ), and 2.9–4.6  $\mu$ s for singlet oxygen ( ${}^1\text{O}_2$ ) [15,16]. To enhance catalytic efficiency, strategies that minimize the migration distance of ROS to target organic molecules are advantageous [17]. In catalytic membrane filtration systems, contaminants are concentrated near the catalyst surface as the feed solution flows through the active layer of the membrane, traversing channels between catalysts. This proximity facilitates a higher concentration of ROS near the catalyst surface, thus leading to more efficient contaminant degradation [7]. As reported, membranes composed of reduced graphene oxide–iron nanoparticle composites have demonstrated the ability to activate PMS and degrade trichloroethylene with over 85% efficiency, while the iron leaching was pretty high [18]. Li et al. [19] constructed catalytic membranes using CoFe Prussian blue analog sheets for the flow-through degradation of antibiotic pollutants, achieving instant removal rates of norfloxacin exceeding 85% for 1 h. However, the leaching concentrations of Co and Fe ions were approximately 4.8 mg/L and 0.3 mg/L, respectively, which is suboptimal for practical applications due to the potential environmental and health risks associated with heavy metal leaching. To address these challenges, it is imperative to develop systems that combine high pollutant removal efficiency with low metal ion leaching for sustainable long-term operation. The robust chemical bonds between metal atoms and their carriers in single-atom catalysts (SACs), facilitated by electronic metal–carrier support interactions (EMSI), significantly bolster electron transfer and enhance catalyst stability [20]. Studies have demonstrated that SACs possess superior catalytic capabilities for degrading organic micropollutants compared to traditional nanocatalysts [21,22], marking them as promising candidates for next-generation water treatment technologies.

In this study, we aimed to develop an effective catalytic membrane based on polytetrafluoroethylene (PTFE) microfiltration membranes for persulfate–AOPs. The iron zeolitic imidazolate framework (Fe ZIF) was employed as a precursor to synthesize an iron–carbon–nitrogen mixture (Fe–NC), which was subsequently converted into an Fe single-atom catalyst (Fe SAC) through an acid leaching treatment. Given the extensive use of nitenpyram (NPR) in agriculture and horticulture, its resistance to natural degradation, and its persistence in the environment, NPR has become a prevalent pollutant [23,24]. The relevant references illustrated that long-term or repeated exposure to NPR can lead to chronic toxicity in mammals [25,26]. In this study, the catalytic activity of Fe-based catalytic membranes was evaluated using NPR as a model organic pollutant within a continuous flow-through system. The dissolution of iron ions and the impact of external water conditions on the removal performance of NPR were investigated. To decipher the reaction mechanisms within the heterogeneous persulfate system, the X-ray photoelectron spectroscopy (XPS), electron spin resonance (EPR), and quenching tests were conducted. This study aims to construct an efficient heterogeneous reaction system for the Fenton-like system application to real-world environmental problems.

## 2. Experimental section

### 2.1. Materials

PMS was purchased from Aladdin Chemistry Co., Ltd. NPR ( $\text{C}_{11}\text{H}_{15}\text{ClN}_4\text{O}_2$ ) was obtained from Alta Scientific Co., Ltd. (Tianjin, China). The iron nitrate solution ( $\text{Fe}(\text{NO}_3)_3$ ), zinc nitrate hexahydrate ( $\text{Zn}(\text{NO}_3)_2 \cdot 6 \text{ H}_2\text{O}$ ), 2-methylimidazole (2-MIM,  $\text{C}_4\text{H}_6\text{N}_2$ ), and tetrabutylammonium bromide (TBAB,  $\text{C}_{16}\text{H}_{16}\text{BrN}$ ) were brought from Sinopharm Chemical Reagent Co., Ltd. The natural organic matter (NOM), potassium hydroxide (KOH), sulfuric acid ( $\text{H}_2\text{SO}_4$ ), potassium phosphate ( $\text{K}_3\text{PO}_4$ ), potassium hydrogen phosphate ( $\text{K}_2\text{HPO}_4$ ), monopotassium phosphate ( $\text{KH}_2\text{PO}_4$ ), potassium bicarbonate ( $\text{KHCO}_3$ ), potassium carbonate ( $\text{K}_2\text{CO}_3$ ), potassium chloride (KCl), potassium sulfate ( $\text{K}_2\text{SO}_4$ ), calcium sulfate ( $\text{CaSO}_4$ ), magnesium sulfate ( $\text{MgSO}_4$ ), potassium iodide (KI), methyl alcohol ( $\text{MeOH}$ ,  $\text{CH}_3\text{OH}$ ), tert-butyl

alcohol (TBA,  $\text{C}_4\text{H}_{10}\text{O}$ ), ethanol ( $\text{EtOH}$ ,  $\text{CH}_3\text{CH}_2\text{OH}$ ), and furfuryl alcohol (FFA,  $\text{C}_5\text{H}_6\text{O}_2$ ) were purchased from Sinopharm Chemical Reagent Co., Ltd. All chemicals were of analytical grade and used without further purification.

### 2.2. Preparation of catalysts and catalytic membranes

The Fe–NC and Fe SAC catalysts were prepared using a co-precipitation method. An amount of 1.5 g of  $\text{Zn}(\text{NO}_3)_2 \cdot 6 \text{ H}_2\text{O}$  was dissolved in 100 mL of water referred to as solution A and 101.3 mg of  $\text{Fe}(\text{NO}_3)_3$  was dissolved in 25 mL of water marked as solution B. Next, 2-MIM (11.25 g) and TBAB (25 mg) were added into 125 mL of water by ultrasonic treatment to form a uniform dispersion, denoted as solution C. Solution A was then added to solution C with stirring for 1 h followed by the addition of solution B, which was stirred for 2 h. The obtained powder was collected by centrifugation, then dried in a vacuum oven at 60°C for 12 h, and named Fe ZIF (Scheme 1, Step 1). As for Step 2 (Scheme 1), the Fe ZIF powder was placed in a quartz boat at 910°C for 2 h under  $\text{N}_2$  in a tube furnace to obtain Fe–NC. The Fe–NC powder would be soaked in 1 M HCl solution at 80°C for 4 h to prepare Fe SAC (Scheme 1, Step 3).

Fe–NC and Fe SAC would be immobilized on the PTFE to prepare Fe–NC and Fe SAC membrane, respectively. For the Fe SAC membrane, 15 mg of Fe SAC powder was dispersed in 100 mL of water using ultrasonic treatment for 60 minutes (Scheme 1, Step 4). The resulting suspension was then passed through a PTFE membrane with a pore size of 0.45  $\mu\text{m}$ , effective diameter of 3.9 cm, and loading of 1.26 mg/cm<sup>2</sup>, using continuous vacuum filtration (Scheme 1, Step 5) for 30 min. The Fe-based membrane was then removed and placed in a drying oven at 60°C for 2 h (Scheme 1, Step 6).

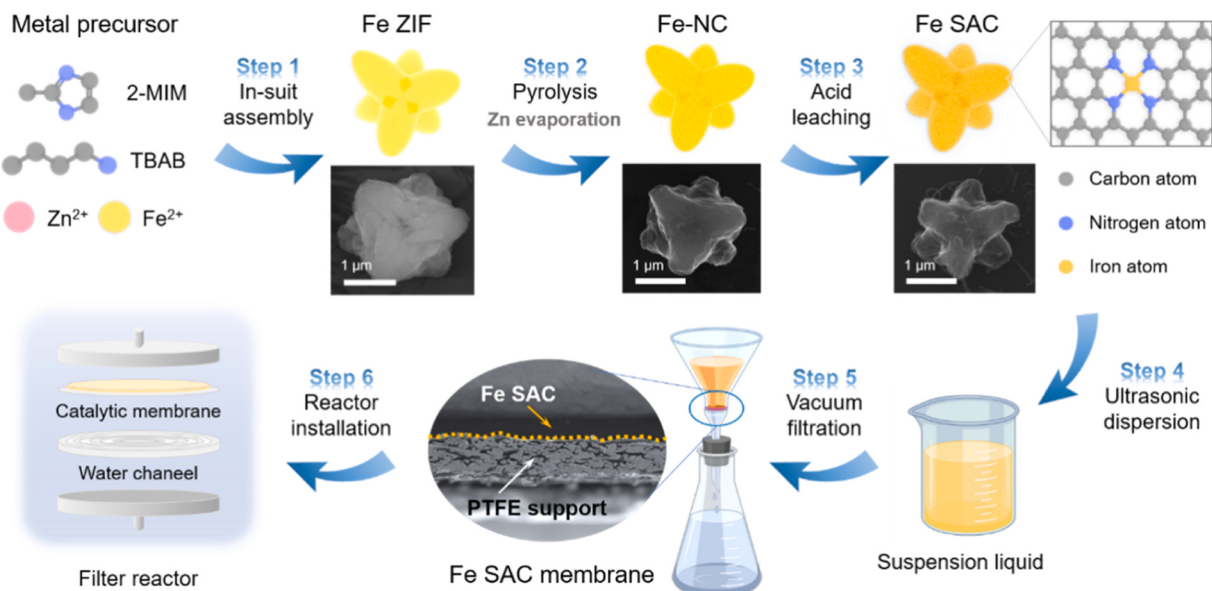
### 2.3. Characterization and theoretical calculation methods of catalysts

High-angle annular dark-field scanning transmission electron microscopy (HAADF–STEM) was performed by FEI Themis Z. X-ray absorption spectroscopy (XAS) of Fe k edge was measured at the Institute of High Energy Physics Chinese Academy of Sciences. An electron paramagnetic resonance (EPR) spectrometer (Japan Electronics JES FA200) in continuous wave X-band mode was used to identify the dominant ROS. 5,5-dimethyl-1-pyrroline-N-oxide (DMPO) was used to capture  $\text{SO}_4^{\bullet-}$ ,  $\bullet\text{OH}$  and  $\bullet\text{O}_2^-$ , and 2,2,6,6-tetramethyl-4-piperidone (TEMP) was used to detect  ${}^1\text{O}_2$ . DMPO or TEMP solution was mixed with catalysts and PMS, and the reaction was initiated. At specific time intervals, 1 mL of the suspension was collected from the catalytic degradation system and filtered through a 0.22  $\mu\text{m}$  filter. The filtered sample was then collected in a quartz capillary tube to detect the corresponding signals. More information of the characterization methods was given in Text S1.

All the calculations were performed using the density functional theory (DFT) with the projector augmented plane-wave (PAW) method, as implemented in the CASTEP package [27,28]. The generalized gradient approximation (GGA) proposed by Perdew, Burke, and Ernzerhof (PBE) was selected as the exchange–correlation potential [28, 29]. The cut-off energy for plane wave was set to 500 eV. A Monkhorst-Pack ( $3 \times 3 \times 1$ ) k-point was used to sample the Brillouin zone. The convergence accuracy for the total energy between electronic steps was set to 10–6 eV for self-consistent field calculations. The van der Waals effect was found to be important in the system being studied. To accurately account for weak interactions and dispersion, the TS method for DFT-D correction was used. The supercell box was kept fixed while all atoms were allowed to fully relax until the residual force per atom was less than 0.03 eV/ $\text{\AA}$ .

### 2.4. Catalytic activity evaluation

The catalytic membrane was installed in the filter reactor (Scheme 1,



**Scheme 1.** Schematic of the preparation strategy for Fe SAC and Fe SAC membrane.

Step 6) to activate PMS in the continuous flow mode (Fig. 1a). The activation performance experiment was conducted at 25°C with an initial pH of 5.50–6.50 for the NPR aqueous solution (1 mg/L). The model wastewater was stored in 5 L brown glass bottles and continuously fed into the column at a flow rate of 11.5 L/d using a peristaltic pump. Simultaneously, a PMS stock solution (1 M) was continuously fed into the sand column at a flow rate of 0.057 L/d. The water quality parameters of different real natural waters were shown in Table S1. For the suspension liquid reaction system, 5.0 mg of catalyst and 1 mL of PMS (0.05 M) were added into 100 mL NPR solution. The effluent (2 mL) was filtered through a 0.22 μm filter, and quenched by adding 20 μL of sodium thiosulfate (1 M) to detect the pollutant concentration at given time intervals. The concentrations and degradation products of NPR were determined by ultra-performance liquid chromatography tandem mass spectrometry (UPLC-MS/MS), with detailed conditions provided in Text S2.

The degradation of contaminants was fitted using pseudo-first-order kinetics, and the corresponding calculation was listed as follows:

$$\ln(C/C_0) = -k_{\text{obs}} \times t$$

Where C<sub>0</sub> and C are the concentrations of pollutants at initial and specified time (t); k<sub>obs</sub> is the pseudo-first-order kinetic rate constant (min<sup>-1</sup>).

The value of the normalization calculation process of k<sub>obs</sub> (k<sub>per M</sub>) was calculated as follows:

$$k_{\text{per } M} = k_{\text{obs}} \times M_{\text{Fe}} / (m_{\text{cat}} \times \text{wt}\%)$$

where m<sub>cat</sub> is the concentration of the catalyst (g/L), M<sub>Fe</sub> = 55.9 g/mol, wt% is the Fe element mass percent.

The calculation process of various ROS contributions was introduced in Text S3. DFT calculations were utilized in this study to identify the active sites of NPR, as described in Text S4.

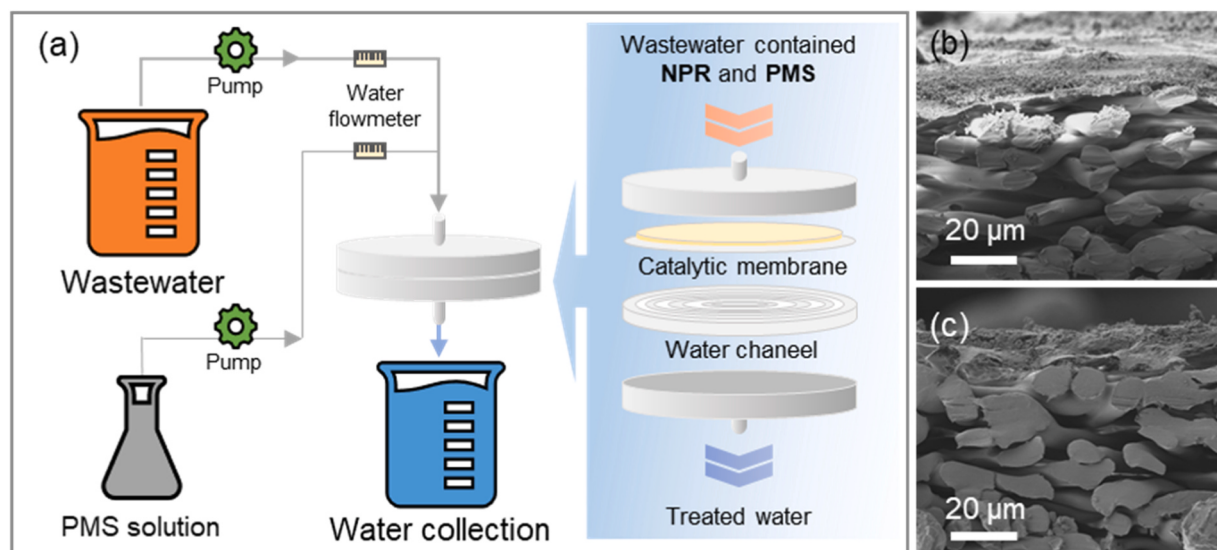


**Fig. 1.** (a) Schematic illustration of wastewater treatment process; The cross-sectional SEM images of (b) Fe SAC membrane and (c) Fe-NC membrane.

### 3. Results and discussion

#### 3.1. Organic pollutant degradation by catalytic membranes

The surface of the PTFE membrane exhibited a flat and smooth morphology with a uniform and well-aligned pore structure, demonstrating high porosity (Figure S1a). The cross-sectional SEM image of PTFE showed that the membrane was composed of fibers (Figure S1b). The cross-sectional SEM images of Fe-NC and Fe SAC catalytic membranes were presented in Fig. 1b–c, showing that the catalyst particles were uniformly deposited on the surface of the PTFE.

Fig. 2a showed the removal efficiency of NPR in the PTFE/PMS system and the PTFE membrane adsorption system, confirming that the pristine PTFE membrane had poor PMS activation and NPR adsorption capacities. The Fe-NC membrane/PMS and Fe SAC membrane/PMS systems exhibited the significant NPR removal performance (Fig. 2a), demonstrating that the powder catalyst supported on the surface of the PTFE membrane played a crucial role in activating PMS. The Fe-NC membrane achieved 98.1% removal of NPR at 60 min, but the removal efficiency decreased to 36.4% at 600 min. The iron dissolution concentration in the treated water samples during continuous dynamic membrane catalysis ranged from 162.62 to 773.73 µg/L (Fig. 2b). The dissolution of metal ions led to the loss of reactive sites, and consequently reduced NPR degradation efficiency. The potential secondary water contamination caused by metal ion dissolution is a common concern in water purification. Using single-atom catalysts instead of nanocrystals may be a solution to reduce secondary metal pollution. As

displayed in Fig. 2a, the Fe SAC membrane exhibited an extremely high instantaneous NPR removal efficiency (>90%) during the continuous filtration process for 600 min. The adsorption capacity of the Fe SAC membrane contributed minimally to the NPR removal (Fig. 2a). This showed that the NPR removal primarily relied on the oxidation effect of ROS, which was generated from the heterogeneous PMS activation process. During the continuous operation for 600 min, the iron leaching concentration of the Fe SAC membrane ranged from 2.85–8.05 µg/L, which was much lower than that of the Fe-NC membrane (Fig. 2b). The metal dissolution concentration was within the limits recommended of Chinese Standards for Drinking Water Quality (GB 5749–2022, ≤300 µg/L) [30,31], proving that the Fe SAC membrane posed little risk of heavy metal pollution. As shown in Fig. 1b and S2, the SEM images of Fe SAC membrane before and after application showed no significant changes, proving the structural stability of Fe SAC catalyst and composite membrane. As summarized in Table S3, the pollutant removal performance of the Fe SAC catalytic membrane system was good, and the metal dissolution concentration was lower than those of previously reported catalytic membranes.

The degradation performance of the Fe SAC membrane/PMS system was evaluated in various water matrices, including tap water, Yellow River water, and Yangtze River water, as shown in Fig. 2c. Over 600 minutes of continuous filtration, the Fe SAC membrane/PMS system consistently achieved more than 80% degradation of NPR from these diverse aquatic environments, highlighting its robust performance and potential applicability in real-world water treatment settings. Furthermore, the Fe SAC PTFE/PMS system was tested against a spectrum of

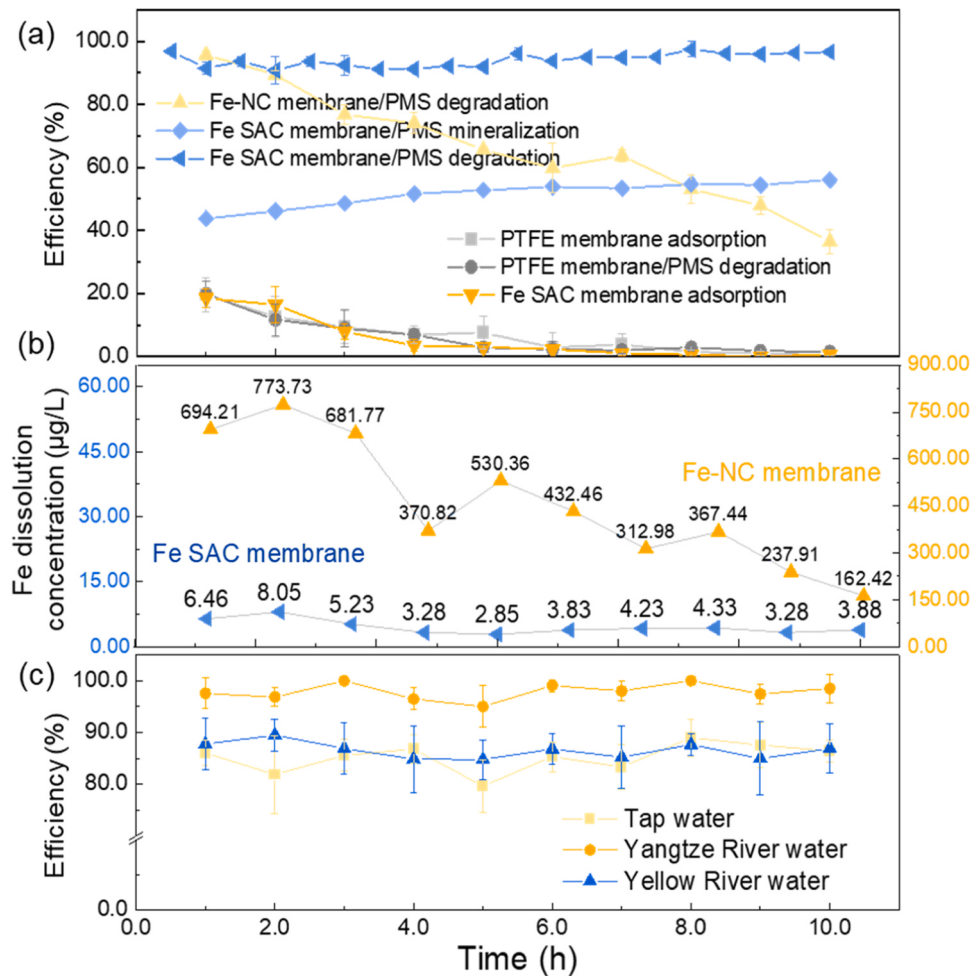


**Fig. 2.** (a) The NPR removal efficiency in various PMS activation systems and adsorption reaction systems; (b) The Fe leaching concentration of the Fe SAC membrane/PMS and Fe NC membrane/PMS systems; (c) The NPR removal efficiency of Fe SAC membrane/PMS in natural water.

structurally diverse refractory organic pollutants, including bisphenol A, sulfamethoxazole, methylene orange, and sulpiride. As exhibited in Figure S3, the results demonstrated the broad-spectrum efficacy of this heterogeneous system, which was critical for addressing the wide range of contaminants encountered in environmental remediation. These findings suggested that the Fe SAC membrane, with its high catalytic activity and stability, could serve as a scalable solution for enhancing the degradation of persistent organic pollutants in various aquatic systems.

### 3.2. Characterizations of catalysts

It was proved that the powder catalyst supported on the surface of PTFE membrane played a crucial role in the PMS activation process. The physicochemical state of the powder catalyst was systematically characterized by analyzing its crystal structure and chemical composition. The Fe ZIF, Fe-NC and Fe SAC all possessed a similar morphology structure of a unique 3D star-like shape consisting of six equal branches (Scheme 1). The synergistic impact of the space-confinement within micropores and the dilution effect exerted by Zn led to the creation of a predominantly mesoporous structure. Most significantly, this interplay guaranteed the stabilization of single-atom-centered sites as opposed to the formation of nanoparticles [32,33]. The Fe content in Fe-NC was 184.271 mg/g (18.43 wt%). After the acid leaching treatment, the metal

content significantly dropped to 15.234 mg/g (1.52 wt%). The Fe content normalized degradation rate ( $k_{per\ M}$ ) was used to evaluate the catalytic performance of Fe-based catalysts. Based on the results shown in Figure S4, the  $k_{per\ M}$  values of Fe-NC and Fe SAC were calculated as 601.8 and 5148.7 min<sup>-1</sup>•mol<sup>-1</sup>, respectively. The result further confirms that the enhanced activity of Fe SAC results from the intrinsic catalytic activity of the active site, rather than from an increase in metal loading content. As exhibited in Table S4, the Fe SAC obtained in this study demonstrated a higher  $k_{per\ M}$  value than other state-of-art SACs regarding the removal of organic pollutants, indicating that Fe SAC exhibits significant reactivity with PMS.

X-rays diffraction (XRD) analysis (Fig. 3a and S5) revealed multiple diffraction peaks in the spectrum of Fe-NC, indicative of the formation of crystalline iron carbide (JCPDS PDF#84-0283 and 77-0225). No characteristic peaks of Fe-containing minerals were present in the XRD spectrum of Fe-SAC, suggesting that the particle size of Fe-SAC was below 1 nm, which was the detection limit for nanocrystalline structures in XRD [12]. This result suggested that the Fe nanocrystals were removed from the catalyst via acid leaching treatment. The dispersion of single Fe atoms anchored on porous N-doped graphene was distinctly observed via high-angle annular dark-field scanning transmission electron microscopy (HAADF-STEM) (Fig. 3b). Though a small number of Fe atoms gathered to form Fe clusters locally in the catalyst. It is

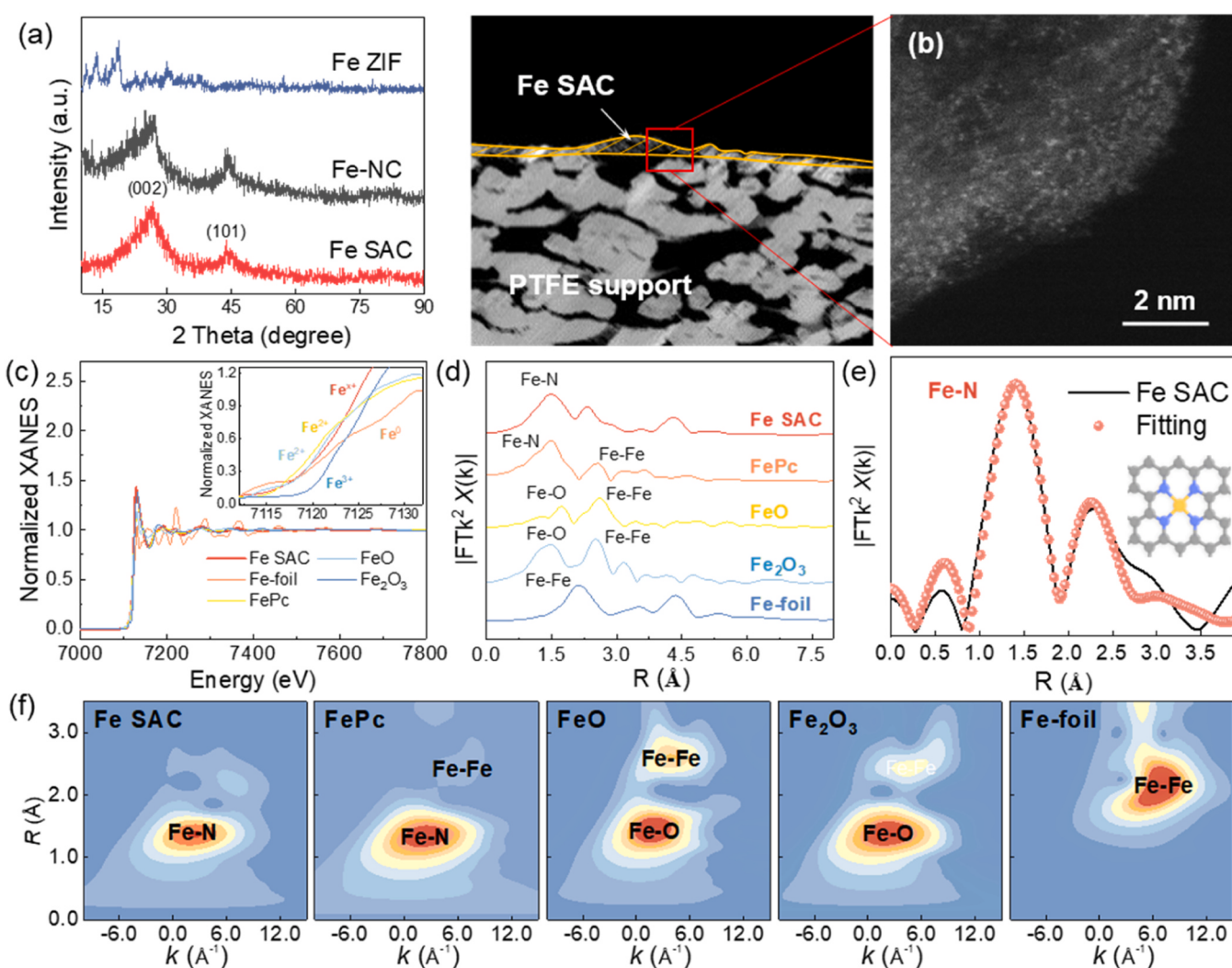


**Fig. 3.** (a) XRD spectra of Fe catalysts; (b) HAADF-STEM of Fe SAC; (c) XANES spectra of Fe k-edge; (d) The Fourier-transformed  $k^3$ -weighted spectra from Fe k-edge EXAFS; (e) Corresponding fitting curves of the EXAFS spectra in Fe SAC at R-space [inset: molecular model of the FeN<sub>4</sub> site in Fe SAC, Atom key: C (gray), N (blue), and Fe (yellow)]; (f) WT-EXAFS plots of Fe SAC, FePc, FeO, Fe<sub>2</sub>O<sub>3</sub>, and Fe-foil.

crucial to note that the predominant species within the Fe SAC were indeed single Fe atoms, as evidenced by the X-ray absorption near edge structure (XANES) spectra of the Fe k-edge (Fig. 3c), the Fourier-transformed  $k^3$ -weighted spectra from the Fe k-edge extended X-ray absorption fine structure (EXAFS) (Fig. 3d), and the corresponding fitting curves of the EXAFS spectra in Fe SAC at R-space (Fig. 3e). The absorption–edge position of Fe SAC overlapped with that of the FePc sample (Fig. 3c), indicating that the Fe valence state in Fe SAC is approximately +2. To further analyze the coordination around the Fe centers, the  $k^3$ -weighted Fourier transform spectra of the Fe k-edge EXAFS are presented in Fig. 3d. The presence of a Fe–N scattering peak at approximately 1.5 Å was recorded, clearly distinguishing it from the Fe–Fe coordination peak at about 2.1 or 2.5 Å in the Fe nanocrystals. EXAFS fitting results identified the average N coordination number as 3.91 for a single Fe atom, forming FeN<sub>4</sub> configurations within the atomically dispersed Fe catalysts (Fig. 3e). Wavelet transforms (WT) of the EXAFS plots, which distinguish backscattering atoms and provide information about coordination structures, were employed for intuitive analysis, as shown in Fig. 3f. Fe SAC exhibited a distinct intensity peak at approximately 2.6 Å<sup>-1</sup>, corresponding to Fe–N coordination. The

characterization analysis confirmed that Fe species are atomically distributed in Fe SAC, forming Fe–N–C structures without the presence of nanocrystals.

As shown in Figure S6 and Table S5, C–C/C=C/C–N was the predominant component on the surface of Fe–NC and Fe SAC, resulting from the transformation of the ZIF framework into C–N functional groups during the pyrolysis process. The XPS spectra of N1s of Fe–NC and Fe SAC exhibited four distinct fitting peaks at 398.2 eV, 400.1 eV, 401.0 eV, and 402.7 eV, respectively (Figure S7). These peaks correspond to pyridinic N, pyrrolic N, graphitic N, and N–oxide, respectively. Figure S7 illustrated a significant increase in the content of pyridinic N and graphitic N following the acid leaching treatment, which likely introduces more defect N–edges or oxygen hole sites in the catalyst [34]. The characteristic peak at 399.0 eV was attributed to the metal–coordinated N (M–Nx), indicating the formation of Fe–N bond (Figure S7). Fe 2p XPS analysis of Fe SAC confirmed the valence state of Fe as +2 (Figure S8). The absence of Fe<sup>0</sup> peaks suggests a high degree of coordination between Fe and N, rather than the formation of Fe–Fe bonds. The characteristic peaks of Fe 2p<sup>3/2</sup> and Fe 2p<sup>1/2</sup> at 713.1 and 725.0 eV can be observed in the Fe 2p XPS spectra of Fe–NC (Figure S8),

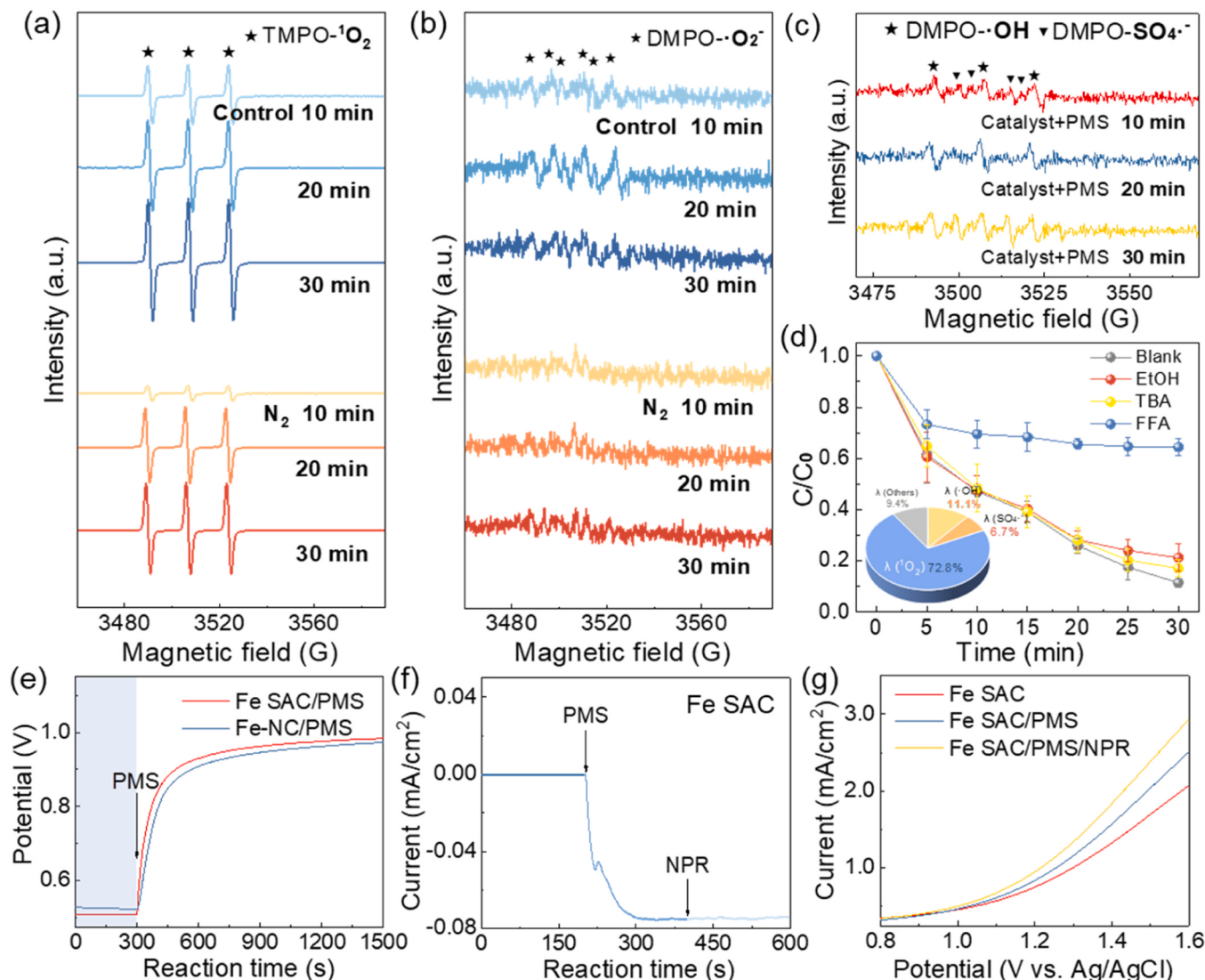


**Fig. 4.** (a)–(c) EPR spectra of Fe SAC/PMS system (Reaction conditions:  $[DMPO \text{ or } TEMP]_0 = 0.1 \text{ M}$ ,  $[\text{Catalyst}] = 0.05 \text{ g/L}$ ,  $[\text{PMS}]_0 = 0.5 \text{ mM}$ , unadjusted pH, and at room temperature); (d) Comparison of reaction rate by corresponding quenching reagents (Reaction conditions:  $[\text{NPR}]_0 = 1 \text{ mg/L}$ ,  $[\text{Catalyst}] = 0.05 \text{ g/L}$ ,  $[\text{PMS}]_0 = 0.5 \text{ mM}$ ,  $[\text{Scavenger}]_0$  listed in figure, unadjusted pH, and at room temperature); Measurement of electron–transfer regime by (e) OCP, (f) chronoamperometry curves, and (g) LSV.

confirming that the iron element existed in the form of +2 and +3 valence. It was inferred that  $\text{Fe}_2\text{O}_3$  nanocrystals and N-coordinated Fe atomic sites were present in Fe-NC, consistent with the XRD results.

### 3.3. Identification of oxidation pathway

EPR and quenching tests were conducted to investigate ROS generation in PMS systems. In the PMS system, the characteristic signals of DMPO-•OH, DMPO- $\text{SO}_4^{\bullet-}$ , DMPO-• $\text{O}_2^-$ , and TEMP- $^1\text{O}_2$  could not be observed due to the self-decomposition of PMS (Figure S9). Upon introducing Fe SAC, the significant TEMP- $^1\text{O}_2$  signals were observed (Fig. 4a). The intensity of TEMP- $^1\text{O}_2$  signal increased significantly as the reaction continued, indicating continuous PMS activation by Fe SAC to form  $^1\text{O}_2$ . Conversely, the intensity of the DMPO-• $\text{O}_2^-$  signals decreased noticeably (Fig. 4b). This decrease was attributed to the transformation of • $\text{O}_2^-$  from dissolved oxygen by the radical secondary reactions and electron transfer in persulfate AOPs. Subsequently, • $\text{O}_2^-$  can serve as an intermediate transforming into  $^1\text{O}_2$  [1,35,36]. As shown in Fig. 4a and 4b, the EPR signals intensity of  $^1\text{O}_2$  slightly decreased after  $\text{N}_2$  treatment, whereas the DMPO-• $\text{O}_2^-$  signals decreased dramatically, indicating that only a part of  $^1\text{O}_2$  was generated by • $\text{O}_2^-$  [3]. The presence of low-intensity septet peaks (hyperfine coupling constants of  $\alpha_{\text{N}} = 7.3 \text{ G}$ ,  $\alpha_{\text{H}} = 3.9 \text{ G}$ ) observed in Fig. 4c indicated minimal •OH and  $\text{SO}_4^{\bullet-}$  in Fe SAC/PMS. Figure S10 exhibited the EPR signals spectra of Fe-NC/PMS system, confirming significant radical generation in the heterogeneous PMS activation system but minimal singlet oxygen formation.

Quenching tests, using NPR as a model pollutant, were conducted to further investigate the generation and roles of ROS in the Fe SAC/PMS and Fe-NC/PMS systems. The addition of tert-butyl alcohol (TBA, a scavenger for •OH) and ethanol (EtOH, a scavenger for both •OH and  $\text{SO}_4^{\bullet-}$ ) slightly hindered NPR degradation in the Fe SAC/PMS (Fig. 4d and S11), implying a minor contribution from •OH and  $\text{SO}_4^{\bullet-}$  [37,38]. Significant effects on NPR degradation were observed following the addition of furfuryl alcohol (FFA, radical scavenger for  $^1\text{O}_2$ , •OH, and  $\text{SO}_4^{\bullet-}$ ) (Fig. 4d and S11). Calculations indicated that the contribution of  $^1\text{O}_2$ , •OH, and  $\text{SO}_4^{\bullet-}$  in the Fe SAC/PMS system was approximately 72.8%, 11.1%, and 6.7%, respectively (inset of Fig. 4d) [39]. In the Fe-NC/PMS system, as depicted in Figure S12, the inhibitory effects of EtOH on the NPR degradation process were comparable to those observed with FFA addition. The quenching experiment results confirmed that NPR removal in these systems relied on radical oxidation, aligning with the findings from EPR analysis. Because the lifetime of  $^1\text{O}_2$  in  $\text{D}_2\text{O}$  (20–32  $\mu\text{s}$ ) is notably longer than in water (around 2  $\mu\text{s}$ ) [40]. This distinction was clearly depicted in Figure S13, where the degradation rate constant of NPR in the Fe SAC/PMS system increased from  $0.070 \text{ min}^{-1}$  to  $0.083 \text{ min}^{-1}$ . The NPR degradation rate in the Fe-NC/PMS system remained relatively unchanged. These results further confirm that the Fe SAC/PMS system degrades NPR through both radical and nonradical oxidation processes, while the Fe-NC/PMS system relies primarily on radical oxidation.

As displayed in Fig. 4e, the open-circuit potential (OCP) analysis indicated that Fe SAC formed a stronger substitutable intermediate (Fe SAC/PMS\*), leading to an elevated oxidation potential and initiating the electron transfer between catalysts and PMS. The role of direct electron transfer in NPR removal within the Fe SAC/PMS system was analyzed using chronoamperometry and linear sweep voltammetry (LSV) [41, 42]. The chronoamperometry curves in Fig. 4f demonstrate that current intensity varied significantly with the addition of PMS, whereas the subsequent addition of NPR had minimal impact on current levels. This result confirmed that the Fe SAC/PMS\* intermediate formed on the surface of Fe SAC, though electron transfer involving PMS/NPR and Fe SAC/NPR was minimal. The LSV curves of Fe SAC/PMS and Fe SAC/PMS/NPR systems were similar, yet both exhibited higher values than the bare Fe SAC system (Fig. 4g). Electron transfer from PMS to the Fe single atoms was observed, and the addition of NPR had negligible

impact on this process, indicating that NPR degradation is largely independent of direct electron transfer.

### 3.4. Discussion of ROS generation mechanism

In the Fe SAC-activated PMS system, the dominant ROS was confirmed as  $^1\text{O}_2$ , with EPR analysis determining that only a portion of  $^1\text{O}_2$  originated from • $\text{O}_2^-$ . Figure S14 showed that the  $\text{N}_2$  treatment did not affect the degradation efficiency or rate of NPR, suggesting that the oxygen in singlet oxygen did not originate from dissolved oxygen, but rather from PMS. The formation pathways of singlet oxygen were explored in the radical and nonradical synergistic oxidation system using theoretical calculation.

DFT calculations were performed to investigate the adsorption and decomposition of PMS on the surface of Fe SAC. As shown in Figure S15, the Bader charges of atoms were calculated to quantitatively describe the electronic density of atoms in Fe SAC and the charge transfer between PMS and catalyst. The charges on the coordinating C and N atoms were significantly lower than those on the Fe atomic sites, indicating superior electron density at the single metal atom sites of Fe SAC. It was further revealed that PMS preferentially bound to the FeN4 site via an O atom from the  $\text{SO}_4^-$  group, forming  $\text{HSO}_5^*$  (Fig. 5a). The  $\text{HSO}_5^*$  then spontaneously split into  $\text{OH}^*$  or  $\text{SO}_4^{\bullet-}$  moieties, facilitating the immediate generation of ROS. As further proved via the partial density of states (PDOS, Fig. 5b), the  $d$ -band center level of Fe in FeN4 was  $-2.52 \text{ eV}$ , which was shifted to the Fermi level relative to  $-1.39 \text{ eV}$  in  $\text{FeN4}-\text{SO}_4^-$ . Conversely, the  $d$ -band center level of  $\text{FeN4}-\text{OH}^*$  moved toward the opposite direction, indicating an increase in  $d$ -band center. PDOS analysis indicated that PMS adsorption altered the electronic structure of Fe atom, with  $\text{FeN4}-\text{SO}_4^-$  showing a stronger interaction than  $\text{FeN4}-\text{OH}^*$  (Fig. 5b). PDOS and Gibbs free energy calculations confirmed that  $\text{HSO}_5^*$  preferred to transform into  $\text{SO}_4^{\bullet-}$ , which was absorbed on the FeN4 site and was released exothermically as  $\text{SO}_4^{\bullet-}$ . This then reacted with hydroxyl ions ( $\text{OH}^-$ ) to generate hydroxyl radicals ( $\text{SO}_4^{\bullet-} + \text{OH}^- \rightarrow \bullet\text{OH} + \text{SO}_4^{2-}$ ) [43]. The Gibbs free energy calculations for the singlet oxygen generation pathways ( $\text{PMS} \rightarrow \text{OH}^* \rightarrow \text{O}^* \rightarrow ^1\text{O}_2$  and  $\text{PMS} \rightarrow \text{OH}^* \rightarrow \text{O}^* \rightarrow \text{OOH}^* \rightarrow ^1\text{O}_2$ ), as shown in Fig. 5a and reported in previous study [44], indicated that these reactions were thermodynamically unfavorable at the FeN4 site.

To determine the singlet oxygen generation mechanism in Fe SAC/PMS, the change in iron valence during the catalytic process was examined. As shown in Fig. 5c, the valence state of Fe maintained as +2 after 10-hour continuous flow experiment. This observation suggests that a valence change occurred in the metal composition during the PMS activation process to produce radicals ( $\text{Fe}^{2+} + \text{HSO}_5^- \rightarrow \text{Fe}^{3+} + \text{SO}_4^{\bullet-} + \text{OH}^-$ ) [3]. XPS analysis further indicated that Fe SAC gained electrons during the reaction with PMS ( $\text{Fe}^{3+} + \text{e}^- \rightarrow \text{Fe}^{2+}$ ) [45]. As depicted in Fig. 5d, the chemical adsorption occurred between PMS and the Fe site, resulting in the transfer of 0.15 electrons from  $^*\text{HSO}_5$  to FeN4. Electrochemical measurements further confirmed the transfer of electrons from PMS to the Fe single atoms (Fig. 4e and 4g). Overall, both experimental results and theoretical calculations demonstrated that the strong chemisorption and electron transfer between PMS and FeN4 facilitated the generation of  $^1\text{O}_2$ , thereby circumventing the Haber-Weiss competitive reaction [39].

### 3.5. Identification of NPR degradation product

Figure S16 illustrated the distribution of the highest occupied molecular orbital (HOMO) of the NPR molecule, highlighting sites prone to electron escape. The electronic density also revealed the reactive sites of NPR, and the structure of the pyridine ring was relatively stable. The nitro group ( $-\text{NO}_2$ ), acting as a strong electron-withdrawing group, shifted the electron cloud distribution within the molecular structure. Near the nitro group, the electron cloud density of the carbon atom decreases, increasing its reactivity. During oxidative decomposition, this

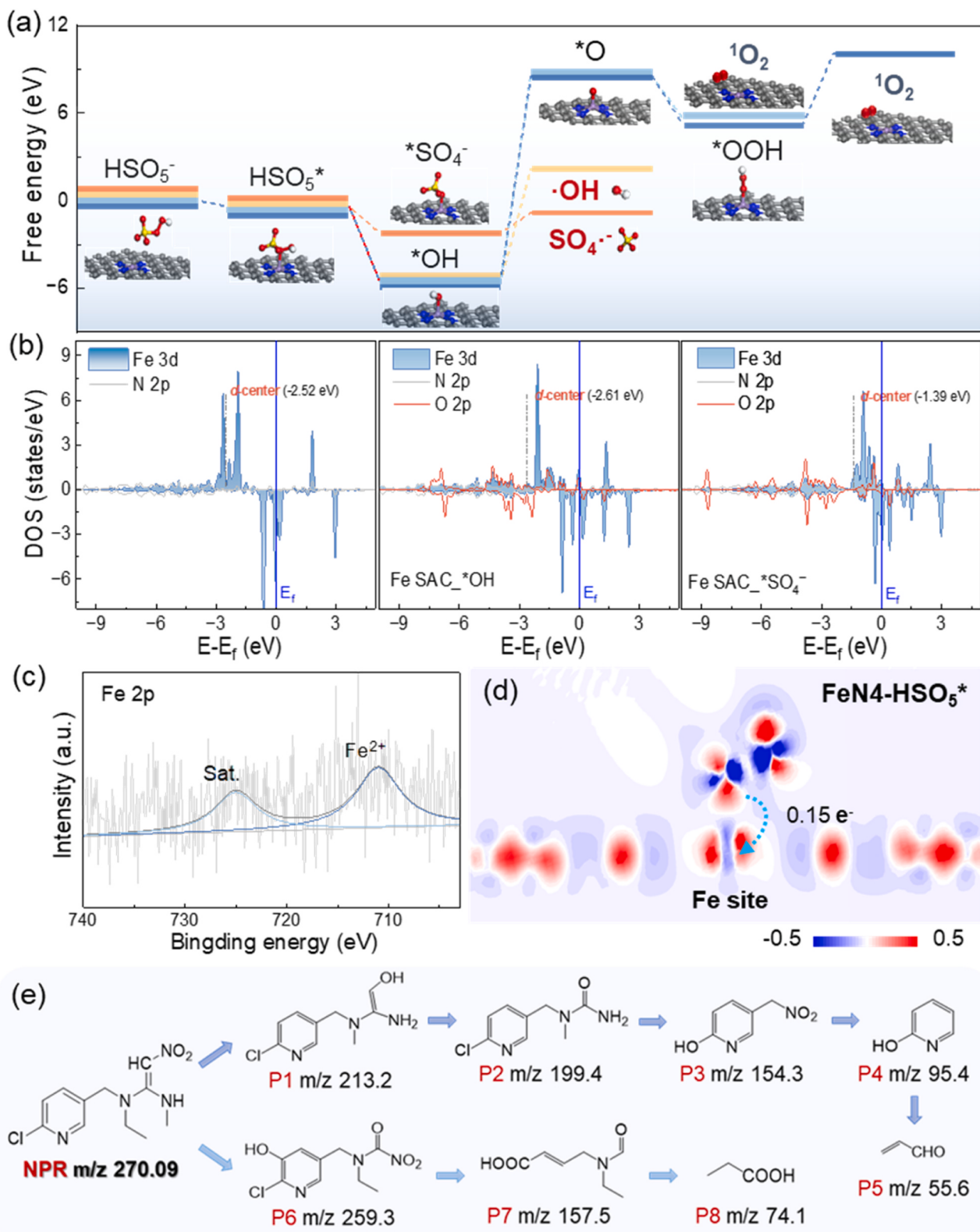


**Fig. 5.** (a) Energy comparison for different PMS activation reaction pathway on the FeN4; (b) PDOS of Fe atom and N atom in FeN4, FeN4-\*OH, and FeN4-\* $\text{SO}_4^-$ , and O atom of PMS in FeN4-\*OH and FeN4-\* $\text{SO}_4^-$ ; (c) Fe 2p XPS spectrum of used Fe SAC; (d) The electron density difference of FeN4-\* $\text{HSO}_5^*$ ; (e) The degradation pathway of NPR in the Fe SAC/PMS system.

C atom is susceptible to oxidative attack. These findings are consistent with our previously published analysis of NPR molecular Fukui index calculations [46].

Degradation intermediates of NPR in the heterogeneous PMS system

were identified. As listed in Table S6 and Figure S17, 9 and 10 intermediates of NPR were detected in the Fe SAC membrane/PMS and Fe SAC/PMS system, respectively. The decomposition pathways of NPR were proposed and shown in Fig. 5e. The electronic density analysis

indicated that the carbon atom bonded to  $\text{--NO}_2$ , when oxidized by  $\bullet\text{OH}$  at the olefinic double bond, formed P1 ( $m/z$  213.3), as previously reported in various AOP studies [47,48]. The compound was further oxidized to produce P2 ( $m/z$  199.4). In the powder catalyst system, NPR and its intermediates, P1 ( $m/z$  213.3) and P2 ( $m/z$  199.4), convert into P2b ( $m/z$  130.1) via a substitution reaction. The Cl atom on the pyridine ring can also be substituted, generating P3 ( $m/z$  154.3). P4 ( $m/z$  95.4) was transformed from P3 ( $m/z$  154.3) through the denitration reaction, followed by ring opening and further oxidation reactions to produce small molecular organic pollutants ( $m/z$  55.6). The N atom in  $\text{--NH--CH}_3$  structure was susceptible to be attacked via denitration and substitution reactions, and  $\bullet\text{OH}$  addition on the pyridine ring occurred due to the high reactivity of  $\bullet\text{OH}$ . This led to the formation of P6 ( $m/z$  259.3), followed by the oxidative ring opening and denitration reactions forming P7 ( $m/z$  157.5). The C–C bond was further oxidized to generate P8 ( $m/z$  74.1). As detected, the concentration of  $\text{NO}_3^-$  and  $\text{Cl}^-$  in the treated water was 0.626 ppm and 0.096 ppm, respectively. Combined with the results of NPR mineralization in the system (Fig. 2a), the oxidation of ROS, which was generated from the heterogeneous PMS activation process, effectively broke down NPR into small organic molecules,  $\text{CO}_2$ , and  $\text{H}_2\text{O}$  effectively.

In the assessment of acute toxicity, the  $\text{LC}_{50}$  values of fish and daphnid, as well as the  $\text{EC}_{50}$  value of green algae, were used as toxicity indicators. For chronic toxicity evaluation, the ChV values of fish, daphnid, and green algae were employed [49]. As shown in Table S7 and Figure S18, except for compound P5 ( $m/z$  55.6) exhibiting higher toxicity than the NPR molecule, the acute toxicity and chronic toxicity of another oxidation intermediates were lower than those of NPR. Overall, the results suggested a significant reduction in the toxicity of NPR following its oxidative degradation by Fe SAC/PMS.

#### 4. Conclusions

Fe SAC was immobilized on the surface of a PTFE membrane to create a catalytic membrane for PMS activation. Compared to nanoparticle Fe catalysts (Fe–NC) membrane/PMS, the Fe SAC membrane/PMS system demonstrated a significantly higher instantaneous NPR removal efficiency (>90%) and lower iron leaching concentrations (2.85–8.05  $\mu\text{g/L}$ ) over a continuous 10-hour filtration process. This membrane proved effective in degrading NPR in various complex aqueous environments, such as tap water, Yellow River water, and Yangtze River water. In the Fe SAC/PMS system, the contribution to NPR removal from  ${}^1\text{O}_2$ ,  $\bullet\text{OH}$ , and  $\text{SO}_4^{2-}$  were approximately 72.8%, 11.1%, and 6.7%, respectively. Electrochemical measurements and theoretical calculations indicated that  ${}^1\text{O}_2$  generation stemmed from strong chemisorption and electron transfer between PMS and FeN4. At the FeN4 site, PMS spontaneously splits into  $\text{SO}_4^{2-}$ , and  $\bullet\text{OH}$  was generated via the reaction between  $\text{SO}_4^{2-}$  and  $\text{OH}^-$ . NPR decomposition occurred through substitution, denitration, and ring-opening reactions within the heterogeneous PMS activation system. This study clarified the reaction mechanisms, including PMS activation, ROS generation, and NPR decomposition, and highlighted the potential of single-atom catalysts in advanced oxidation processes for water remediation.

#### CRediT authorship contribution statement

**Jian Xu:** Writing – review & editing, Supervision, Project administration, Conceptualization. **Ruonan Guo:** Writing – original draft, Methodology, Investigation. **Changsheng Guo:** Writing – review & editing, Methodology. **Zenghui Bi:** Methodology, Investigation. **Heng Zhang:** Investigation. **Ningqing Lv:** Writing – review & editing, Investigation. **Beidou Xi:** Writing – review & editing, Methodology. **Guangzhi Hu:** Supervision, Methodology.

#### Declaration of Competing Interest

The authors declare that they have no known competing financial interests or personal relationships that could have appeared to influence the work reported in this paper.

#### Data Availability

No data was used for the research described in the article.

#### Acknowledgments

This work was funded by the National Science Fund for Distinguished Young Scholars (42325706) and National Natural Science Foundation of China (42177382).

#### Appendix A. Supporting information

Supplementary data associated with this article can be found in the online version at doi:10.1016/j.apcatb.2024.124243.

#### References

- [1] R. Guo, B. Xi, C. Guo, N. Lv, J. Xu, Comprehensive insight into heterogeneous persulfate activation for environmental pollutants degradation: Approaches and mechanism, *Environmental Functional Materials*, (2022).
- [2] F. Chen, G. Huang, F. Yao, Q. Yang, Y. Zheng, Q. Zhao, H. Yu, Catalytic degradation of ciprofloxacin by a visible-light-assisted peroxymonosulfate activation system: performance and mechanism, *Water Res.* 173 (2020) 115559.
- [3] N. Li, J. Ye, H. Dai, P. Shao, L. Liang, L. Kong, B. Yan, G. Chen, X. Duan, A critical review on correlating active sites, oxidative species and degradation routes with persulfate-based antibiotics oxidation, *Water Res.* 235 (2023) 119926.
- [4] H. Li, N. Yuan, J. Qian, B. Pan, Mn2O3 as an electron shuttle between peroxymonosulfate and organic pollutants: the dominant role of surface reactive Mn(IV) species, *Environ. Sci. Technol.* 56 (2022) 4498–4506.
- [5] J. Qi, X. Yang, P. Pan, T. Huang, X. Yang, C. Wang, W. Liu, Interface engineering of  $\text{Co(OH)}_2$  nanosheets growing on the  $\text{KNbO}_3$  perovskite based on electronic structure modulation for enhanced peroxymonosulfate activation, *Environ. Sci. Technol.* 56 (2022) 5200–5212.
- [6] Y.-d. Chen, R. Wang, X. Duan, S. Wang, N. Ren, S. Ho, Production, properties, and catalytic applications of sludge derived biochar for environmental remediation, *Water Res.* 187 (2020) 116390.
- [7] R. Guo, B. Xi, C. Guo, X. Cheng, N. Lv, W. Liu, A.G.L. Borthwick, J. Xu, Persulfate-based advanced oxidation processes: the new hope brought by nanocatalyst immobilization, *Environ. Funct. Mater.* 1 (2022) 67–91.
- [8] B.C. Hodges, E.L. Cates, J. Kim, Challenges and prospects of advanced oxidation processes using catalytic nanomaterials, *Nat. Nanotechnol.* 13 (2018) 642–650.
- [9] X. Yang, A. Wang, B. Qiao, J. Li, J. Liu, T. Zhang, Single-atom catalysts: a new frontier in heterogeneous catalysis, *Acc. Chem. Res.* 46 (2013) 1740–1748.
- [10] Y. Shang, X. Xu, B. Gao, S. Wang, X. Duan, Single-atom catalysis in advanced oxidation processes for environmental remediation, *Chem. Soc. Rev.* 50 (2021) 5281–5322.
- [11] R. Guo, Z. Bi, B. Xi, C. Guo, N. Lv, G. Hu, J. Xu, Co single-atom catalyst outperforms its homogeneous counterpart for peroxymonosulfate activation to achieve efficient and rapid removal of nitenpyram, *Chem. Eng. J.* 483 (2024) 149269.
- [12] W. Ma, M. Sun, D. Huang, C. Chu, T. Hettke, X. Wang, Y. Zhao, J. Kim, M. Elimelech, Catalytic membrane with copper single-atom catalysts for effective hydrogen peroxide activation and pollutant destruction, *Environ. Sci. Technol.* 56 (2022) 8733–8745.
- [13] Y. Chen, G. Zhang, H. Liu, J. Qu, Confining free radicals in close vicinity to contaminants enables ultrafast fenton-like processes in the interspacing of  $\text{MoS}_2$  membranes, *Angew. Chem. Int. Ed.* 58 (2019) 8134–8138.
- [14] A. Cruz-Alcalde, N. López-Vinent, R.S. Ribeiro, J. Giménez, C. Sans, A.M.T. Silva, Persulfate activation by reduced graphene oxide membranes: practical and mechanistic insights concerning organic pollutants abatement, *Chem. Eng. J.* 427 (2022) 130994.
- [15] V. Amaral-Rogers, L.P. Belzunges, M.F. Bijleveld van Lexmond, J.M. Bonmatin, M. Chagnon, C.A. Downs, L. Furlan, D.W. Gibbons, C. Giorio, V. Girolami, D. Goulson, D.P. Kreutzweiser, C. Krupke, M. Liess, E. Long, M. McField, P. Mineau, E.A. Mitchell, C.A. Morrissey, D.A. Noome, L. Pisa, J. Settele, N. Simon-Delso, J. Stark, A. Tapparo, H. Van Dyck, J. van Praagh, P.R. Whitehorn, M. Wiemers, Conclusions of the worldwide integrated assessment on the risks of neonicotinoids and fipronil to biodiversity and ecosystem functioning, *Environ. Sci. Pollut. Res.* 22 (2014) 148–154.
- [16] F. Chen, L. Liu, J. Wu, X. Rui, J. Chen, Y. Yu, Single-atom iron anchored tubular  $\text{g-C}_3\text{N}_4$  catalysts for ultrafast fenton-like reaction: roles of high-valency iron-oxo species and organic radicals, *Adv. Mater.* 34 (2022).

[17] X. Li, X. Huang, S. Xi, S. Miao, J. Ding, W. Cai, S. Liu, X. Yang, H. Yang, J. Gao, J. Wang, Y. Huang, T. Zhang, B. Liu, Single cobalt atoms anchored on porous n-doped graphene with dual reaction sites for efficient fenton-like catalysis, *J. Am. Chem. Soc.* 140 (2018) 12469–12475.

[18] A. Aher, S. Thompson, T. Nickerson, L. Ormsbee, D. Bhattacharyya, Reduced graphene oxide–metal nanoparticle composite membranes for environmental separation and chloro-organic remediation, *RSC Adv.* 9 (2019) 38547–38557.

[19] J. Li, H. Yi, Y. Xiao, C. Liang, Y. Shen, Y. Li, Q. Fang, Freestanding catalytic membranes assembled from blade-shaped Prussian blue analog sheets for flow-through degradation of antibiotic pollutants, *Appl. Catal. B: Environ.* 336 (2023) 122922.

[20] G. Ren, M. Shi, Z. Li, Z. Zhang, X. Meng, Electronic metal-support interaction via defective-induced platinum modified BiOBr for photocatalytic N<sub>2</sub> fixation, *Appl. Catal. B: Environ.* 327 (2023) 122462.

[21] Y. Gao, C. Yang, M. Zhou, C. He, S. Cao, Y. Long, S. Li, Y. Lin, P. Zhu, C. Cheng, Transition metal and metal–Nx codoped MOF-derived fenton-like catalysts: a comparative study on single atoms and nanoparticles, *Small* 16 (2020) 2005060.

[22] P. Yang, Y. Long, W. Huang, D. Liu, Single-atom copper embedded in two-dimensional MXene toward peroxymonosulfate activation to generate singlet oxygen with nearly 100% selectivity for enhanced Fenton-like reactions, *Appl. Catal. B: Environ.* 324 (2023) 122245.

[23] M.L. Hladik, A.R. Main, D. Goulson, Environmental risks and challenges associated with neonicotinoid insecticides, *Environ. Sci. Technol.* 52 (2018) 3329–3335.

[24] Y. Wan, Y. Wang, W. Xia, Z. He, S. Xu, Neonicotinoids in raw, finished, and tap water from Wuhan, Central China: assessment of human exposure potential, *Sci. Total Environ.* 675 (2019) 513–519.

[25] S. Yan, S. Tian, Z. Meng, M. Teng, W. Sun, M. Jia, Z. Zhou, S. Bi, W. Zhu, Exposure to nitenpyram during pregnancy causes colonic mucosal damage and non-alcoholic steatohepatitis in mouse offspring: the role of gut microbiota, *Environ. Pollut.* 271 (2021) 116306.

[26] S. Yan, Z. Meng, S. Tian, M. Teng, J. Yan, M. Jia, R. Li, Z. Zhou, W. Zhu, Neonicotinoid insecticides exposure cause amino acid metabolism disorders, lipid accumulation and oxidative stress in ICR mice, *Chemosphere* 246 (2020) 125661.

[27] G. Kresse, J. Furthmüller, Efficient iterative schemes for ab initio total-energy calculations using a plane-wave basis set, *Phys. Rev. B* 54 (1996).

[28] A. Gk, B. Jf, Efficiency of ab-initio total energy calculations for metals and semiconductors using a plane-wave basis set, *Comput. Mater. Sci.* 6 (1996) 15–50.

[29] J.P. Perdew, K. Burke, M. Ernzerhof, Generalized gradient approximation made simple, *Phys. Rev. Lett.* 77 (1996).

[30] Standards for drinking water quality, GB 5749-2022, Standardization Administration of China, Beijing, 2022.

[31] Y. Zhang, Z. Hou, P. Fu, X. Wang, T. Xue, Y. Chen, Passivation efficiency and mechanism of arsenic-contaminated mining soil with iron-based solid wastes in collaboration with ferrous sulfate, *J. Environ. Chem. Eng.* 11 (2023) 110704.

[32] J. Zhu, M. Xiao, D. Ren, R. Gao, X. Liu, Z. Zhang, D. Luo, W. Xing, D. Su, A. Yu, Z. Chen, Quasi-covalently coupled Ni–Cu atomic pair for synergistic electroreduction of CO<sub>2</sub>, *J. Am. Chem. Soc.* 144 (2022) 9661–9671.

[33] R. Guo, Z. Bi, B. Xi, C. Guo, H. Zhang, N. Lv, G. Hu, J. Xu, A new generation pathway of singlet oxygen in heterogeneous single-atom Mn catalyst/ peroxymonosulfate system, *Chem. Eng. J.* 481 (2024) 148629.

[34] P. Huang, P. Zhang, C. Wang, J. Tang, H. Sun, Enhancement of persulfate activation by Fe-biochar composites: synergism of Fe and N-doped biochar, *Appl. Catal. B: Environ.* 303 (2022) 120926.

[35] Y. Nosaka, A.Y. Nosaka, Generation and detection of reactive oxygen species in photocatalysis, *Chem. Rev.* 117 (2017) 11302–11336.

[36] Y. Zeng, F. Wang, D. He, J. Sun, J. Li, H. Luo, X. Pan, Role of superoxide radical and singlet oxygen in peroxymonosulfate activation by iron-doped bone char for efficient acetaminophen degradation, *Chem. Eng. J.* 459 (2023) 141642.

[37] Y. Cho, R. Lin, Y. Lin, Degradation of 2,4-dichlorophenol by CuO-activated peroxydisulfate: importance of surface-bound radicals and reaction kinetics, *Sci. Total Environ.* 699 (2020) 134379.

[38] J. Wang, Y. Xie, G. Yu, L. Yin, J. Xiao, Y. Wang, W. Lv, Z. Sun, J. Kim, H. Cao, Manipulating selectivity of hydroxyl radical generation by single-atom catalysts in catalytic ozonation: surface or solution, *Environ. Sci. Technol.* 56 (2022) 17753–17762.

[39] L. Zhang, X. Jiang, Z. Zhong, L. Tian, Q. Sun, Y. Cui, X. Lu, J. Zou, S. Luo, Carbon nitride supported high-loading Fe single-atom catalyst for activation of peroxymonosulfate to generate 1O<sub>2</sub> with 100% selectivity, *Angew. Chem. Int. Ed.* 60 (2021) 21751–21755.

[40] Z. Wang, E. Almatrafi, H. Wang, H. Qin, W. Wang, L. Du, S. Chen, G. Zeng, P. Xu, Cobalt single atoms anchored on oxygen-doped tubular carbon nitride for efficient peroxymonosulfate activation: simultaneous coordination structure and morphology modulation, *Angew. Chem. Int. Ed.* 61 (2022) e202202338.

[41] X. Peng, J. Wu, Z. Zhao, X. Wang, H. Dai, Y. Wei, G. Xu, F. Hu, Activation of peroxymonosulfate by single atom Co-N-C catalysts for high-efficient removal of chloroquine phosphate via non-radical pathways: electron-transfer mechanism, *Chem. Eng. J.* 429 (2022) 132245.

[42] Y. Chai, H. Dai, X. Duan, Z. Sun, F. Hu, J. Qian, X. Peng, Elucidation of the mechanistic origin of spin-state-dependent P-doped Fe single-atom catalysts for the oxidation of organic pollutants through peroxymonosulfate activation, *Appl. Catal. B: Environ.* 341 (2024) 123289.

[43] R. Guo, Y. Li, Y. Chen, Y. Liu, B. Niu, J. Gou, X. Cheng, Efficient degradation of sulfamethoxazole by CoCu LDH composite membrane activating peroxymonosulfate with decreased metal ion leaching, *Chem. Eng. J.* 417 (2021) 127887.

[44] Y. Gao, T. Wu, C. Yang, C. Ma, Z. Zhao, Z. Wu, S. Cao, W. Geng, Y. Wang, Y. Yao, Y. Zhang, C. Cheng, Activity trends and mechanisms in peroxymonosulfate-assisted catalytic production of singlet oxygen over atomic metal-N-C catalysts, *Angew. Chem. Int. Ed.* 60 (2021) 22513–22521.

[45] S. Zuo, D. Li, Z. Guan, F. Yang, H. Xu, D. Xia, J. Wan, Tailored d-band facilitating in Fe gradient doping CuO boosts peroxymonosulfate activation for high efficiency generation and release of singlet oxygen, *ACS Appl. Mater. Interfaces* 13 (2021) 49982–49992.

[46] R. Guo, C. Guo, H. Zhang, B. Xi, N. Lv, J. Xu, Enhanced nitenpyram degradation by metallic carbon nitrogen composites catalyzed peroxymonosulfate: synergistic effect of radical and nonradical pathways, *Chem. Eng. J.* 476 (2023) 146483.

[47] Z. Pei, C. Wang, P. Wang, G. Zhou, Covalent-anion-driven self-assembled cadmium/ molybdenum sulfide hybrids for efficient nitenpyram degradation, *J. Environ. Manag.* 316 (2022) 115269.

[48] S. Xiong, H. Zeng, Y. Deng, C. Feng, R. Tang, Z. Zhou, L. Li, J. Wang, D. Gong, Insights into the dual Z-scheme and piezoelectricity co-driven photocatalyst for ultra-speed degradation of nitenpyram, *Chem. Eng. J.* 451 (2023) 138399.

[49] K.S. Tay, N. Madehi, Ozonation of ofloxacin in water: by-products, degradation pathway and ecotoxicity assessment, *Sci. Total Environ.* 520 (2015) 23–31.